

The Airborne Aero-Optics Laboratory, Recent Data

Nicholas De Lucca^{a*}, Stanislav Gordeyev^a and Eric Jumper^a
^aHessert Laboratory, University of Notre Dame, Notre Dame, IN USA 46556

ABSTRACT

In this paper recent in-flight aero-optical measurements on the Airborne Aero-Optics Laboratory (AAOL) will be given. Instrumentation and experimental set-up will be presented. Results of an extensive survey of the aero-optical environment at different viewing angles for both flat-window and conformal-window turrets at different subsonic and low transonic speeds, below $M = 0.65$, will be presented, compared and extensively discussed. The statistical analysis of wavefronts at different viewing angles will also be presented and discussed.

Keywords: Aero-Optics, Turrets, AAOL, Wavefronts, Flight Tests

1. INTRODUCTION

Several flight platforms for laser systems have been developed over the years, from the ALL in the 1970s to the ATL in the 2000s. A common feature of laser projection systems is the hemisphere-on-cylinder turret, a geometry that from a diffraction-limited point of view provides excellent field of regard, but introduces several unique aero-optical problems¹ when used in typical flows around aircraft². As shown in figure 1, the upstream portion of the flow field around the turret is relatively benign; the curvature of the turret induces a favorable pressure gradient that keeps the flow attached. The curvature of the downstream portion of the turret has an opposite effect - an adverse pressure gradient forms which leads to flow separation and the formulation of a highly-turbulent wake. The wake of the turret creates a fluctuating density field that gives rise to index-of-refraction variation in the air. The vortical structures in the wake include two horn vortices. About the base of the cylinder, a necklace vortex forms and propagates downstream. These flow features are dependent on the Reynolds number until a minimum Reynolds number is reached. Additionally, for incoming Mach numbers larger than 0.55, a shock forms over the top of the turret as the flow becomes locally supersonic^{2,3}.

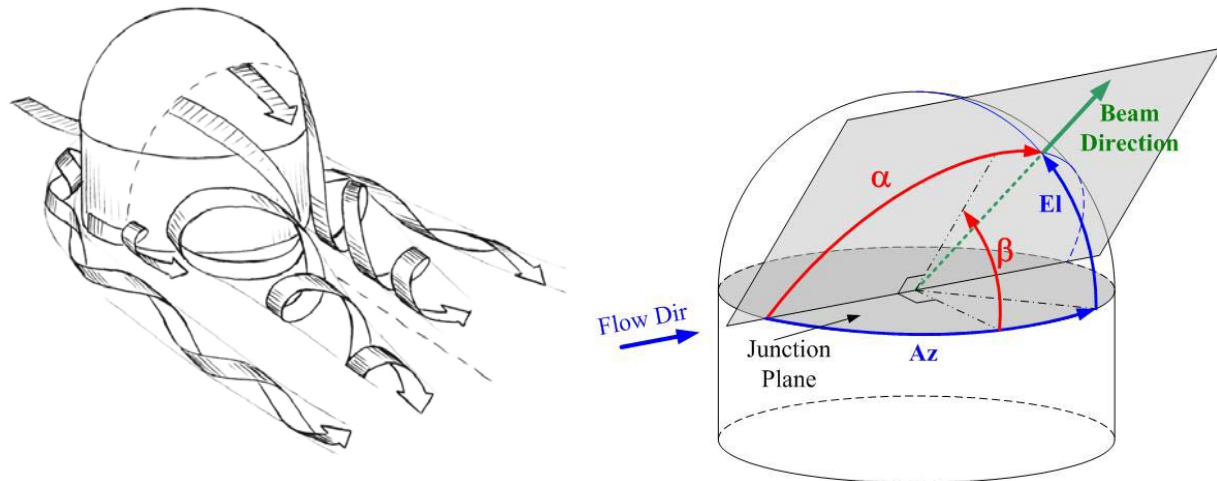


Figure 1. The dominant flow structures around a hemisphere-on-cylinder turret, left and the turret viewing angle definitions, right.

In addition to aero-optical effects, the unsteady pressure field of the flow induces mechanical vibration in the turret which may result in significant beam jitter. These two effects can significantly reduce the far field intensity of the laser and limit the effective field of regard for the turret.

*Corresponding author, E-mail: ndelucca@nd.edu

The turret viewing direction is commonly described with two angles, the azimuthal angle (Az) and the elevation angle (El). From a fluid-flow perspective, a different coordinate system helps to collapse the data and still be able to account for some elevation angle dependence. As shown in figure 1, right, the azimuth and elevation angles are transformed into two new angles, α , the viewing angle and β , the modified elevation angle. The transformation for these two angles is given by $\alpha = \cos^{-1}(\cos(Az)\cos(El))$ and $\beta = \tan^{-1}\left(\frac{\tan(El)}{\sin(Az)}\right)$. The reason for this coordinate change can be demonstrated

using the turret flow field described in figure 1. For pure spheres, the flow field would only be a function of how far upstream or downstream the turret is looking, which is represented by the angle α . The modified elevation angle accounts for changes in the flow that are derived from the symmetry-breaking presence of the cylinder under the hemisphere, the aircraft wall and the existence of the horn vortices mentioned earlier.

2. EXPERIMENTAL SETUP

2.1 Instrumentation

The AAOL provides a flight-test platform for studying these and other aero-optical effects and designing mitigation systems with flow control or adaptive optics. Detailed description of AAOL is provided in Jumper et al.⁴. Here we provide only essential details about the flight experiment. Two aircraft flying in closed formation are used in the AAOL program. The laboratory aircraft holds the turret assembly, mounted to the optical bench inside the aircraft so that it protrudes into the airstream through a modified escape hatch. The various other measurement systems can also be integrated into the escape hatch. The second aircraft flies in close formation with the laboratory aircraft; the second aircraft projects a laser beam onto the laboratory aircraft turret pupil. This source laser is projected out of a window on the source aircraft instead from a second turret, to avoid propagation through non-boundary-layer turbulence. The emitted laser projects through the attached boundary layer as a small beam aperture that is diverging so that by the time it arrives at the laboratory turret it overfills the turret pupil by two times. Because of the initial small beam size and overflow of the laboratory aircraft turret pupil, the tracking requirements for the source beam are somewhat less than that for the turret on the laboratory aircraft.



Figure 2. The AAOL turret with a flat-window (left) and a conformal-window (right) apertures.

An annotated photograph and schematics of the optical bench on the laboratory aircraft are given in Figure 3. The primary sensor on the laboratory aircraft (AAOL) is the high-speed 2-D Shack-Hartmann wavefront sensor, capable of acquiring wavefronts with spatial resolution of 32×32 at 25 kHz. The initial 0.10 m aperture beam is re-imaged to the 0.02 m beam. Additionally, the turret assembly contains a closed-loop Fast Steering Mirror (FSM) system which stabilizes the beam on the sensor. Residual beam jitter is measured by a Position Sensing Device (PSD) on the optical table. In addition to acquiring wavefronts and the residual jitter, instantaneous flight speed, static/total pressures and the

turret’s elevation and azimuth angles were recorded, along with the instantaneous distance between the two aircraft measured via differential GPS. The residual jitter data, flight parameters and turret angles were acquired simultaneously at 100 kHz. The wavefronts and GPS data were collected with separate Data Acquisition Systems at different sampling speeds, but they were synchronized with the jitter data. Although it was acquired during flight tests, the residual jitter and GPS data will not be discussed in this paper. The analysis of the jitter data can be found in the companion paper⁵.

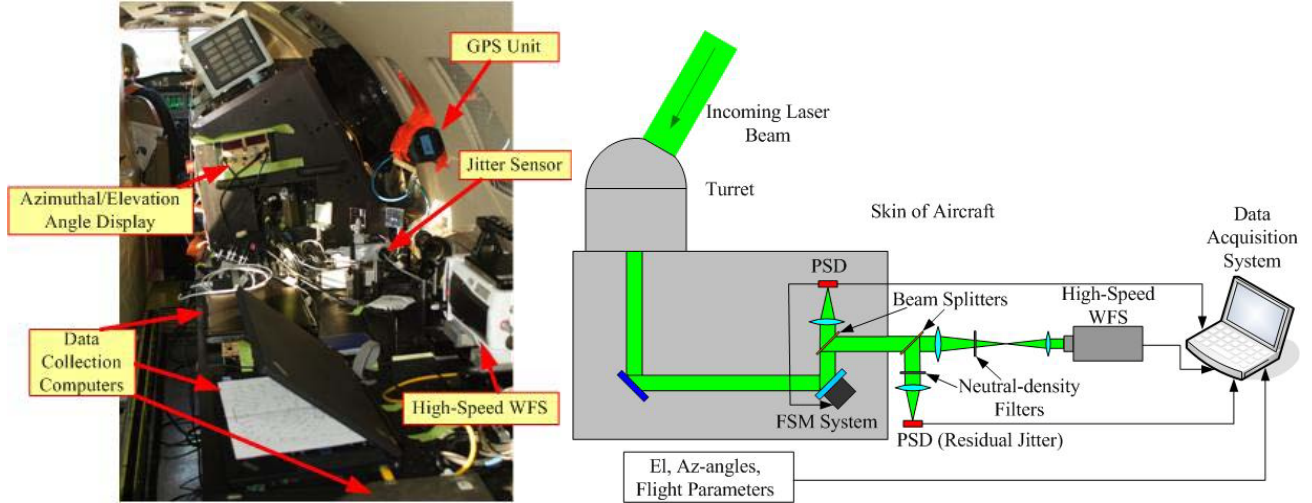


Figure 3. The optical setup on the turret aircraft.

Data were acquired in one of two different modes: a fixed relative aircraft position or a “slew” maneuver. For fixed-position data, wavefronts were acquired at 25 kHz for 15,000 frames. Fixed position data allows collected data at higher sampling frequency for a better time resolution of aero-optical structures. A slewing maneuver involved the source laser aircraft moving slowly and monotonically with respect to the turret aircraft. To enable data acquisition for a longer time period of 7 seconds, the wavefront acquisition rate was reduced to 3 kHz for slewing maneuvers and total of 21,000 wavefronts were acquired per each slew maneuver. Wavefronts collected during slewing maneuvers, while not time-resolved, provided statistical properties of aero-optical distortions over a range of elevation/azimuthal angles and facilitate an overall mapping of the optical performance of the turret over a large field of regard. Flight conditions varied from $M = 0.4$ or $M = 0.5$ at an altitude of 15,000 ft to $M = 0.6-0.65$ at altitudes from 28,000-34,000 ft.

2.2 Wavefront Reduction and Analysis

Processing image data from the high-speed WF sensor provides spatial-temporal-resolved wavefront sequences, $W = W(x, y, t)$. For each wavefront sequence, the steady lensing, instantaneous tip/tilt and instantaneous piston were removed from each wavefront during data reduction. The procedure is slightly different for slewing maneuvers, as will be explained in more detail later in this paper. The Optical Path Difference, OPD , which is the conjugate of the wavefront, is given by $OPD = -W$. Several statistical quantities were calculated from these wavefront sequences. One of them is the instantaneous spatial RMS of the OPD over the aperture, $OPD_{RMS}(t) = \sqrt{\langle OPD(x, y, t)^2 \rangle_{x,y}}$, where angle

brackets denote spatial averaging over the aperture. The time-averaged $OPD_{RMS}(t)$, later in this paper denoted by just OPD_{RMS} , gives the overall value of aero-optical distortions at a given angle. The temporal histogram of instantaneous $OPD_{RMS}(t)$ provides useful information about the temporal deviation around the time-averaged OPD_{RMS} and is also useful for checking data quality. The temporal variation of $OPD_{RMS}(t)$ is quantified by the spread of the $OPD_{RMS}(t)$, defined as $\Sigma = \sqrt{\langle OPD_{RMS}(t) - \overline{OPD_{RMS}} \rangle^2}$, which is the standard deviation of the OPD_{RMS} over its time-averaged value. It is also useful to quantify the spatial distribution of the aero-optical distortions. This is achieved by taking the temporal RMS of the OPD of each fixed point over the aperture, $OPD_{RMS}(x, y) = \sqrt{\langle OPD(x, y, t)^2 \rangle}$, later referred to in this paper as the spatial distribution of OPD_{RMS} .

Before raw images from the high-speed WF sensor were converted into wavefronts, wavefront data quality was checked through several measures. The first series of checks occurs during wavefront data reduction. In Figure 4 an example of a raw image file is presented; it should be noted that this image has been image enhanced so that it is easier to view. Although the Shack-Hartmann sensor is technically intensity-invariant, the intensity of a given dot can vary in time, potentially affecting the data quality. As a result, any location on the image with sufficiently low-intensity can temporally lose enough intensity to make centroid determination inaccurate. To correct for this, dots with very low average intensity were ignored in processing. Additionally, having intensity that is too large will saturate the dot image and reduce the sub-pixel resolution for centroid determination. To avoid this issue, neutral-density filters were, if needed, added to or removed from the optical train in flight to regulate the beam intensity at the sensor.

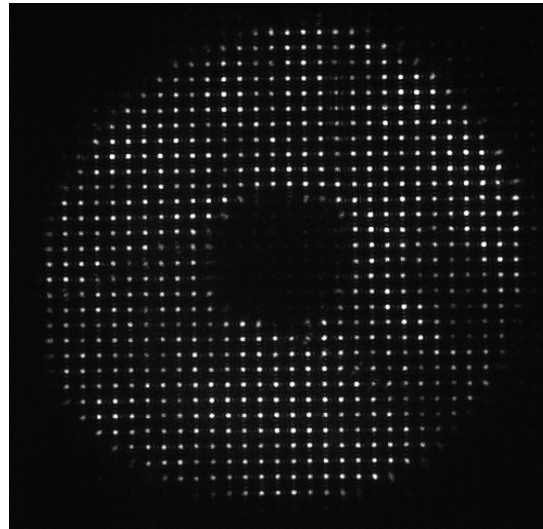


Figure 4. A sample image from the Shack-Hartmann WF sensor.

The mean flow around the turret imposes a density field that lenses the beam. This steady lensing is viewing-angle and elevation-angle dependent. Because the beam train assumes a specific aircraft separation when re-imaging, the steady lensing also has a defocus component, depending on the relative distance between the two aircraft. The strength of this defocus changes over the course of a slew maneuver as aircraft separation does not remain constant. The total steady lensing of the beam is removed for each averaging subset to compensate for both these effects. To eliminate this corrupting effect during a slew maneuver, the slew data series were split into 0.5-second subsets, and average statistics were computed over these subset time periods; thus, the short-time steady lensing and the instantaneous tip/tilt were removed from each 0.5 second subset. The slew rate for the aircraft, in terms of turret rotation, was typically two degrees per second, and as a result, averaging over a half second of data gave results in averaging over a single degree of rotation. Figure 5 shows the statistical convergence of OPD_{RMS} as a function of data set duration. The OPD_{RMS} converges within half a second, confirming that 0.5-second data sequence provides correct statistics of OPD_{RMS} at the viewing angle. As fixed-position data were acquired at 25 kHz for 0.6 seconds, it was not subdivided and the steady lensing across all frames and instantaneous tip/tilt were removed. The full suite of statistics was computed for each fixed-angle data set and each slewing maneuver subset.

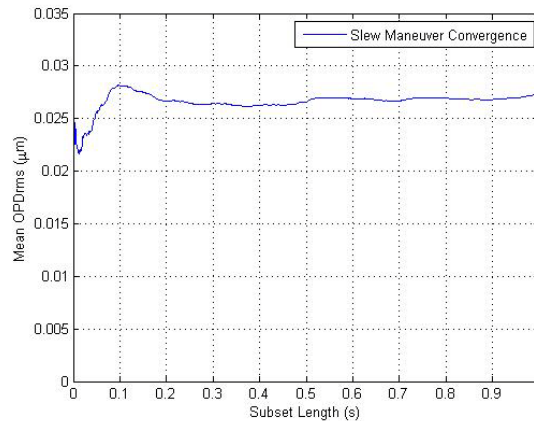


Figure 5. The convergence of OPD_{RMS} for a slew maneuver.

After images from the high-speed WF sensor were converted into wavefront sequences, using commercially available software, various statistical quantities were calculated from them, as discussed earlier. Besides providing important statistical information about aero-optical distortions, these quantities give additional measures of data quality. Figure 6 gives an example of two metrics, the spatial distribution of OPD_{RMS} and probability distribution function of the instantaneous OPD_{RMS} . For the spatial distribution of the OPD_{RMS} at back-looking angles, the linear gradient in the flow

direction is typical of a shear layer formed over the aperture; the downstream portion of the aperture looks through a larger portion of the shear layer than the upstream part, increasing the local OPD_{RMS} . The spatial distribution also does not contain any obvious modes such as a large defocus contribution or any single points that are vastly different from those near it. The histograms of the temporal distribution of OPD_{RMS} typically have a log-normal distribution, as shown in Figure 6, right plot. Wavefronts with unusually-large values of OPD_{RMS} will be present in the histogram as a number of outliers in the distribution tail, which *might indicate* that these wavefronts are corrupted.

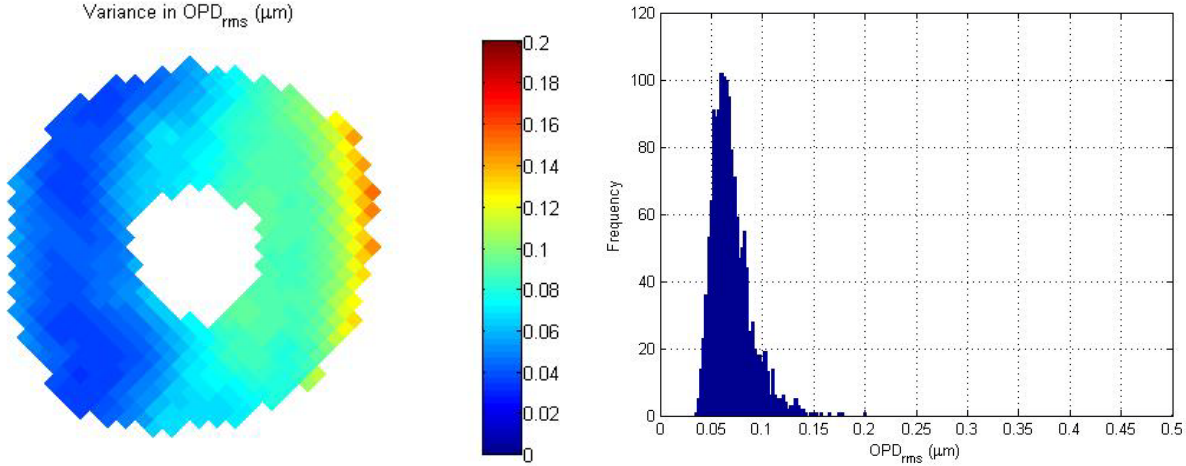


Figure 6: Sample spatial distribution of OPD_{RMS} and histogram of OPD_{RMS} over the aperture. $M = 0.48$, $\alpha = 106^\circ$, $\beta = 62.2^\circ$.

3. RESULTS

3.1 Subsonic Flight Data

To compare the aero-optical environment between flat and conformal turret windows, OPD_{rms} was computed at a large number of azimuth and elevation angles. The OPD_{RMS} values were normalized by flight conditions,

$$OPD_{Norm} \left(\frac{\mu m}{m} \right) = \frac{OPD_{RMS}}{\left(\frac{\rho_0}{\rho_{SL}} \right) M^2 D}$$

Here the free stream density is ρ_0 , while the density at sea level is ρ_{SL} . The diameter of the turret is given by D and M is the free stream Mach number. This scaling was previously shown to correctly normalize aero-optical distortions over turrets for subsonic Mach numbers of 0.4 - 0.5⁶.

Figure 7 presents the measured OPD_{RMS} values for the flat-window (left column) and the conformal-window (right column) turrets in either the Az-El (upper plot) or α - β (lower plot) angular coordinate systems. Figure 8 presents the same data, but with plots of OPD_{RMS} as a function of viewing angle sorted into narrow bands of β . For a range of $50^\circ < \alpha < 70^\circ$ with a flat window and $50^\circ < \alpha < 100^\circ$ with a conformal window, normalized OPD_{RMS} values are in the range of 1 $\mu m/m$, close to the noise level of the sensor, implying that aero-optical environment at these viewing angles is relatively benign. This agrees well with our current understanding of fluid mechanics around turrets; except for looking-forward, low-elevation angles, where the presence of the necklace vortex at the base of the turret introduces additional aero-optical distortions, flow on the forward portion of the turret is attached and only the weak aero-optical effects come from the thin boundary layer⁷ Between $70^\circ < \alpha < 110^\circ$ - 120° for the flat-window turret, typical values of the normalized OPD_{RMS} are larger, in the range of 1.5-2.5 $\mu m/m$, compared to the normalized OPD_{RMS} about 1 $\mu m/m$ for the conformal-window turret, which is around the noise level of the sensor. For these side-looking angles, the slope discontinuity between the turret surface and the flat window will force the formation of a separation bubble over the flat window⁸. The bubble size increases with the increase in the viewing angle, α , consequently increasing OPD_{RMS} , until it peaks near 90° ; the exact location of the peak in OPD_{RMS} was found to be a weak function of the elevation angle. After the OPD_{RMS} peaks, it begins to decrease. This decrease was shown to be a result of the tip/tilt removal from the wavefronts⁸. For the

conformal window, the turret surface does not have any slope discontinuities around the aperture and the flow stays attached at these viewing angles, resulting in low values of OPD_{RMS} . For back-looking angles $\alpha > 110^\circ - 120^\circ$, both the flat and the conformal window have a large increase in OPD_{RMS} , as the flow separates at the back of the both turrets and the laser beam traverses through the turbulent wake. As α continues to increase, normalized OPD_{RMS} increases to a value of $6 \mu\text{m/m}$ for both the flat and conformal windows. The rapid increase occurs as the laser passes through a larger portion of the wake (i.e., slant range through the wake). The separation point, which can be loosely defined as the angle after which OPD_{RMS} begins a sharp rise, occurs at smaller α for higher modified elevation angles for both turrets. This indicates that the separation occurs sooner near the top of the turret. Both the flat and conformal windows also exhibit a drop in OPD_{RMS} values for high elevation angles $\beta > 80^\circ$. For this region close to the centerplane of the turret, the flow is not directly affected by the two horn vortices referred to earlier, see Figure 1, right, and therefore tends to stay attached longer and therefore is less-optically-active².

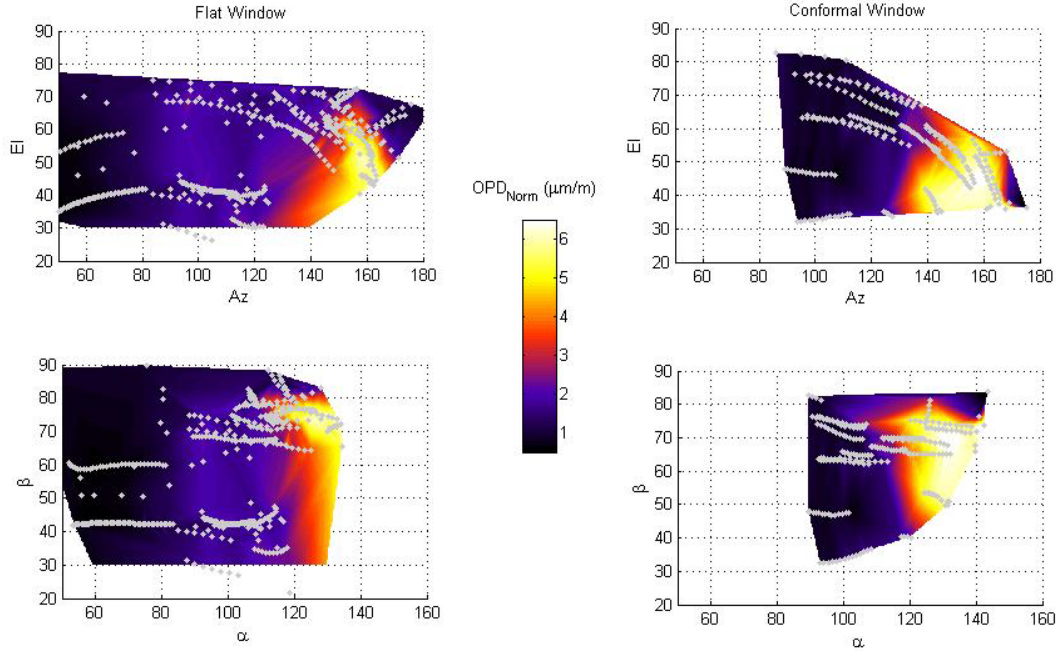


Figure 7. Two dimensional maps of OPD_{RMS} as a function of Az, El and α , β . The grey dots indicate actual data points, values in between are interpolated.

As shown in figure 8, the local maximum of OPD_{RMS} for the flat window between $\alpha = 90$ and 100 degrees is a function of the modified elevation angle. This indicates that the separation bubble formed over the flat window at these side-looking angles is sensitive to the elevation angle and thus the proximity to the aircraft surface. The exterior surface of the aircraft introduces additional flow features like the necklace vortex and formation of the horn vortices, thus preventing the OPD_{RMS} from being solely a function of the viewing angle, α . Except for this separation bubble, the aero-optical behavior of the flat window turret for $\alpha < 80^\circ$ is independent of β . For $\beta > 80^\circ$, OPD_{RMS} values actually decrease; in this region, the turret looks through the comparatively benign area in between the two horn vortices in the wake. The exact separation point has significant β -dependence. This is the point at which the flow doesn't continue to adhere to the surface of the turret; it is the beginning of the wake region. For $\beta < 50^\circ$, flow remains attached at least until $\alpha = 120^\circ$, while separation occurs near $\alpha = 118^\circ$ and $\alpha = 110^\circ$ for $50^\circ < \beta < 70^\circ$ and $70^\circ < \beta < 80^\circ$, respectively.

For the conformal-window turret, aero-optical effects are more independent of β because it lacks the elevation-angle-sensitive separation bubble over the window. The conformal window also exhibits smaller OPD_{RMS} values for $\beta > 80^\circ$, similar to the flat-window turret. The conformal window also displays the same separation point dependence on β , but the flow separates at α values that are 5° smaller for $50^\circ < \beta < 80^\circ$. This indicates that while the flat window has additional aero-optical distortions in the $80^\circ < \alpha < 110^\circ$ range, it slightly improves flow conditions outside of this range. Physically, the curvature of the conformal window induces an adverse pressure gradient that leads to separation. For the flat window, a small separation bubble forms over the window, but at these viewing angles the flow re-attaches shortly

after it, as the adverse pressure gradient due to the slope of the window is not strong enough to cause separation to re-occur before the window's edge. The end result is the delayed formation of the turbulent wake in the vicinity of the flat window.

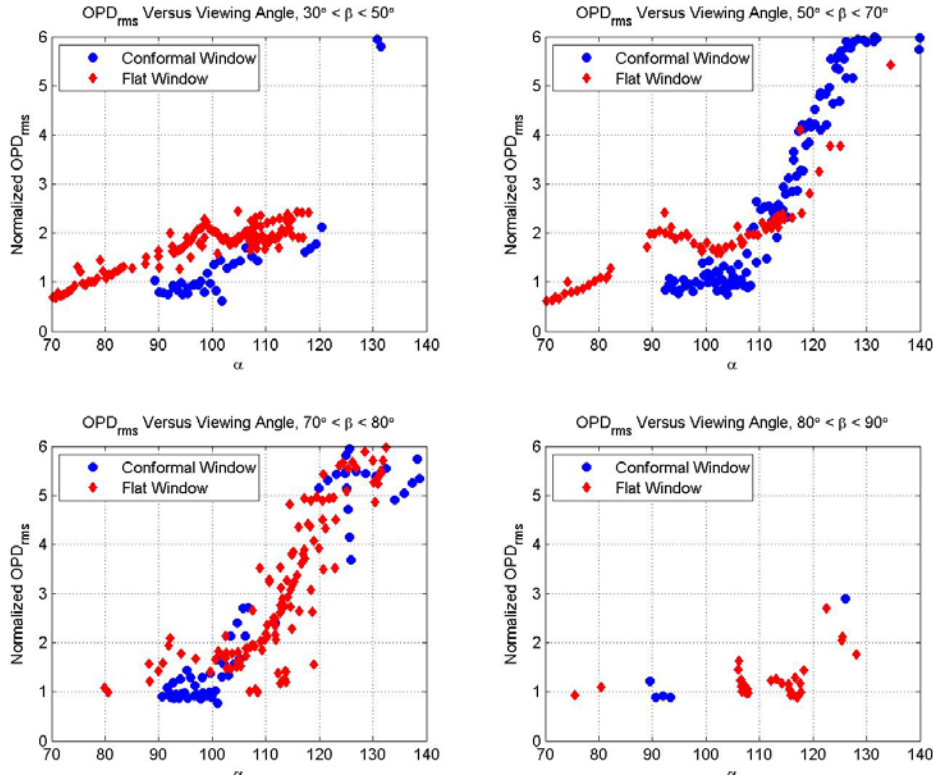


Figure 8. Comparison of mean OPD_{RMS} for flat and conformal windows at different modified elevation angle slices.

3.2 Temporal variation of OPD_{RMS} and communications applications

While the time-averaged OPD_{RMS} directly affects the intensity at the target, OPD_{RMS} varies in time, as can be seen in time histogram, Figure 6, right. In terms of system performance this is indicative of time periods when $OPD_{RMS}(t)$ is larger than the time-averaged OPD_{RMS} , resulting in further decrease in the far-field intensity, a potentially detrimental effect to airborne laser-based communication systems.

To quantify the temporal variation of $OPD_{RMS}(t)$ about the time-averaged OPD_{RMS} , the temporal standard deviation of the mean-removed $OPD_{RMS}(t)$ or spread, Σ , was calculated for all time series for different elevation/azimuthal angles. Results for the conformal window turret, normalized by $(\rho_0 / \rho_{SL})M^2 D$ are presented in Figure 8, left plot, as a function of the viewing angle for the range of $50^\circ < \beta < 80^\circ$. The spread values are low for side-looking angles $\alpha < 110^\circ$ and rapidly increase for higher viewing angles, following the general trend for OPD_{RMS} values in Figure 8, upper right. To confirm this, the spread was normalized by the time-averaged OPD_{RMS} ; these results are plotted in Figure 9, right. Over a wide range of viewing angles the spread was found to be approximately proportional to the OPD_{RMS} , $\Sigma \approx 0.28 \cdot OPD_{RMS}$.

It was shown⁹ that if the wavefront is Gaussian in space, the instantaneous far-field Strehl Ratio depends only on the instantaneous $OPD_{RMS}(t)$, $SR(t) = \exp(-[2\pi OPD_{RMS}(t)/\lambda]^2)$. Analysis of the spatial distributions of the wavefronts for both the flat-window⁷ and the conformal-window turrets revealed that the wavefronts do have a spatial Gaussian distribution for a wide range of elevation/azimuthal angles. Thus, if the temporal distribution of $OPD_{RMS}(t)$ is known, it is possible to predict the probability distribution for the far-field Strehl Ratio¹⁰. Analysis of the temporal distribution of OPD_{RMS} has shown that for subsonic speeds they can be well-approximated by a log-normal distribution,

$\text{PDF}(OPD_{rms}) = \frac{1}{OPD_{rms} s \sqrt{2\pi}} \exp\left[-\frac{(\ln OPD_{rms} - m)^2}{2s^2}\right]$, where parameters m and s are related to time-averaged $\mu = OPD_{RMS}$

and the spread, Σ , as $m = \log\left(\frac{\mu}{\sqrt{1 + (\Sigma/\mu)^2}}\right)$, $s^2 = \log\left(1 + (\Sigma/\mu)^2\right)$. For the conformal-window turret,

$\Sigma \approx 0.28 \cdot OPD_{RMS} = 0.28\mu$, giving $m = \log(0.96\mu)$, $s = 0.18$, and the OPD_{RMS} -probability distribution becomes,

$\text{PDF}(OPD_{rms}) = \frac{1}{0.18\sqrt{2\pi}OPD_{rms}} \exp\left[-\frac{(\ln OPD_{rms} - \log(0.96\mu))^2}{0.066}\right]$. If the far-field intensity threshold is given, one can

predict relative duration of intensity drop-outs due and potentially-lost data due to temporal variation of $OPD_{RMS}(t)$ for different subsonic flight conditions and elevation/azimuthal angles¹⁰.

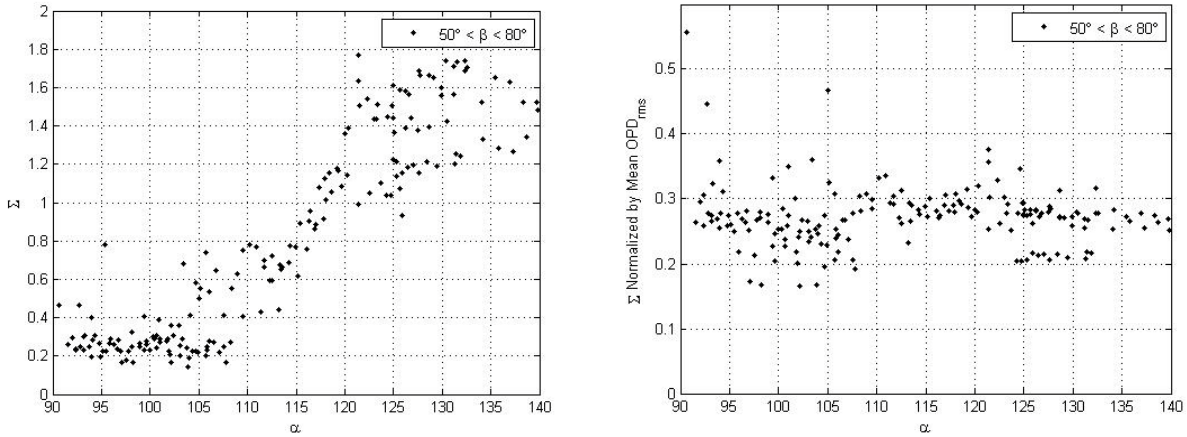


Figure 9. Left: Temporal standard deviation of OPD_{RMS} , Right: Temporal standard deviation of OPD_{RMS} normalized by mean OPD_{RMS} for the conformal window. $M=0.5$

3.3 Transonic Flight Data

For the speeds greater than $M = 0.55$, the flow becomes supersonic on the turret near the top (i.e., transonic), with a terminating shock². To investigate the direct effect of the shock on the aero-optical distortions, wavefronts were measured for side-looking angles, $85^\circ < \alpha < 100^\circ$ (where the shock appears in the aperture); and, also wavefronts were collected at back-looking angles, $100^\circ < \alpha < 130^\circ$ to see the shock effect on the separation region aft of the turret. Results for the conformal-window turret are presented in Figure 10, left plot, for two ranges of the modified elevation angle, $30^\circ < \beta < 50^\circ$ and $50^\circ < \beta < 70^\circ$. Subsonic results are also plotted in Figure 10, left plot, for comparison. The shock creates additional stationary density gradients, which do not affect OPD_{RMS} , as any stationary aero-optical effects are removed from wavefronts when the steady wavefront is subtracted from the wavefront sequences, as described earlier; however, the interaction between the boundary layer and the shock results in the unsteady shock motion, demonstrated in wavefront sequences in Figure 11. This wavefront unsteadiness results in an increase in OPD_{RMS} for side-looking angles, as observed in Figure 10, left plot, for the range of $30^\circ < \beta < 50^\circ$. These additional shock-related aero-optical effects are functions of the modified elevation angle, as OPD_{RMS} results for the range $50^\circ < \beta < 70^\circ$ differ from the results for the range $30^\circ < \beta < 50^\circ$. Detailed analysis of the shock-related spatial/temporal evolution of aero-optical distortions for both the flat-window and the conformal window turrets can be found in Goorskey et. al.¹¹

The shock trips the boundary layer and forces a premature separation to occur on top of the turret, compared to the separation point around 115-120 degrees for the subsonic cases. The premature separation leads to a wider wake downstream of the turret and therefore, levels of aero-optical distortions becoming larger compared to the subsonic cases. Indeed, for back-looking angles normalized values of OPD_{RMS} are larger compared to the normalized values of OPD_{RMS} for the subsonic cases, see Figure 10, left plot.

The comparison between the transonic and subsonic results for the flat-window turret is presented in Figure 10, right plot for different modified elevation angle ranges. For the viewing angle around 90 degrees, the shock significantly modifies

the local separation bubble present over the flat-window aperture, essentially eliminating the bubble-related peak at $\alpha = 100$ degrees present for the subsonic case. Instead, the shock-related effects create additional aero-optical distortions around $\alpha = 90$ degrees for the transonic case. As for the conformal-window turret, the shock-related effects depend on the modified elevation angle, as OPD_{RMS} are different for different β -ranges, see Figure 10, right plot, for α between 85 and 95 degrees. Similar to the conformal-window, the shock also forces a premature separation and a wider wake, leading to higher values of the normalized OPD_{RMS} compared to the subsonic cases.

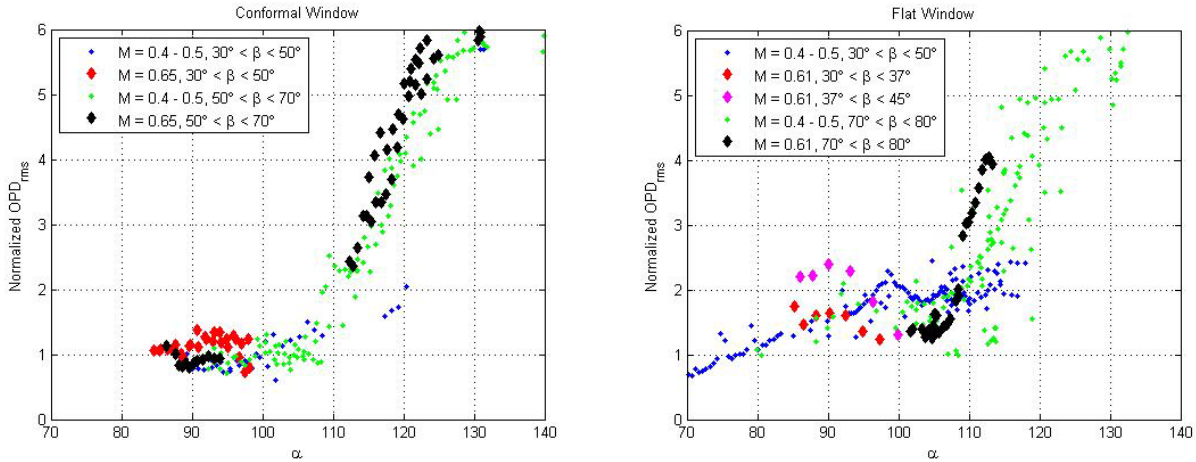


Figure 10. Comparison of transonic and subsonic mean OPD_{RMS} for the conformal-window (left plot) and the flat-window (right plot) turrets.

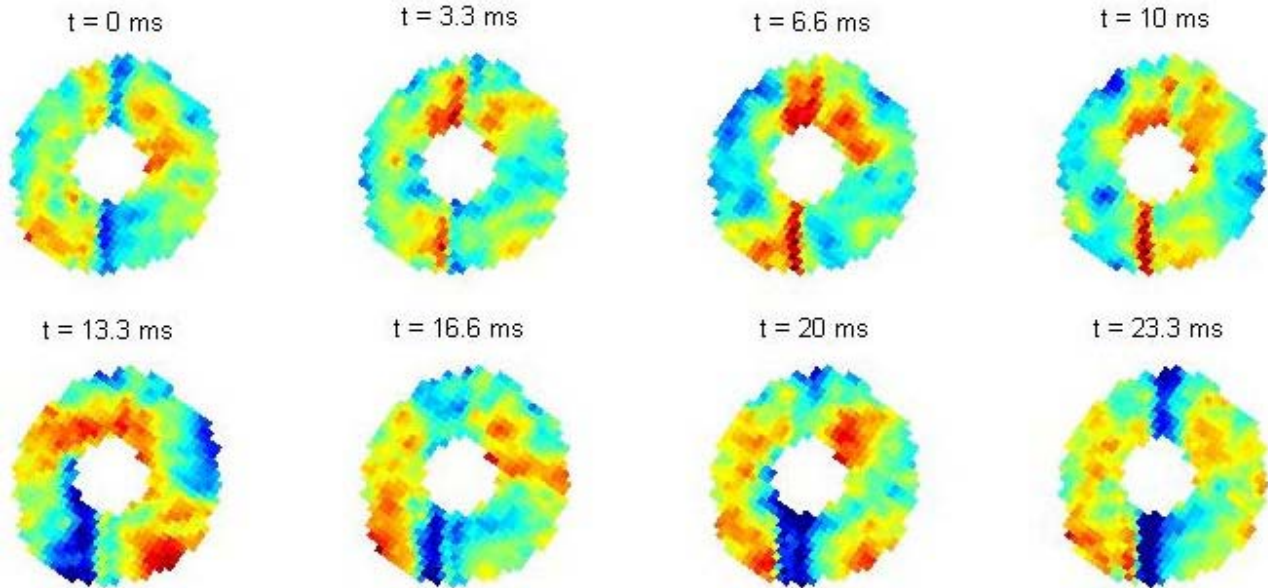


Figure 11. Time evolution of the shock on the aperture. Conformal window turret, $M = 0.6$, $\alpha = 85^\circ$, $\beta = 40^\circ$.

4. CONCLUSIONS

Wavefront measurements were performed on the Airborne Aero-Optics Laboratory (AAOL) for both a flat- and conformal-window turrets. These measurements were obtained for a large range of viewing angles and at both subsonic and transonic speeds. From the wavefronts, mean OPD_{RMS} and the standard deviation of OPD_{RMS} , Σ , were computed to characterize the aero-optical environment.

For a flat-window turret in the subsonic case, the aero-optical environment was shown to be relatively benign for the viewing angles of $50^\circ < \alpha < 70^\circ$ as the flow is attached to the turret and the only aero-optical aberrations come from an attached turbulent boundary layer. The conformal window had the same behavior for $50^\circ < \alpha < 100^\circ$. From $70^\circ < \alpha < 110^\circ$ - 120° , the aero-optical environment for the flat-window turret is dominated by a separation bubble forming over the flat aperture, increasing normalized OPD_{RMS} values compared to the conformal-window turret results over the same range of viewing angles. For both window configurations, the flow exhibits a separation for $\alpha > 100$ - 120° , but the flow separates slightly earlier over the conformal window due to the stronger adverse pressure gradient induced by the window curvature. For the flat-window turret, the wake formation is delayed as flow re-attaches after the separation bubble and the adverse pressure gradient due to the window slope isn't strong enough to cause the separation to occur before the edge of the flat aperture. The dynamics of the separation bubble for the flat-window turret and the location of the separation exhibit a significant dependence on the modified elevation angle β . The flow was shown to separate at smaller α for larger β , except for $\beta > 80^\circ$, where the flow is not directly affected by the horn vortices dominating the wake.

The spread in instantaneous OPD_{RMS} was shown to be approximately proportional to the time-mean value of OPD_{RMS} , $\Sigma \approx 0.28OPD_{RMS}$. Since the spatial OPD -distribution was found to be Gaussian, this relationship can be used to predict the probability distribution of the far-field Strehl Ratio. Given a far-field intensity threshold, the relative duration of intensity drop-outs, and, for communication applications, potential data-losses, can be predicted

For plane Mach numbers larger than 0.55, the flow becomes locally supersonic over the turret, and a shock was shown to form. The interaction of the shock and the boundary causes unsteady shock motion, resulting in an increase of OPD_{RMS} in the $85^\circ < \alpha < 100^\circ$ range; this increase was found to be highly dependent on β . The shock also trips the boundary layer on top of the turret and was shown to force premature separation, increasing the size of the turret wake and further increasing OPD_{RMS} . It was also pointed out that the mean OPD over the aperture when the shock is present over the aperture was removed prior to finding the large unsteady OPD_{RMS} , but the removed OPD contains a large optical discontinuity and optical wedge discontinuity that cannot be neglected.

Future work will include additional studies of the transonic flow regime and an extension of current subsonic scaling laws to transonic speeds. Additionally, analysis will be extended to different turret geometries, such as the hemispheric-only turret. Various forms of flow control that have been previously tested in wind tunnels will be adapted to flight testing and their effect on the aero-optical environment will be studied.

ACKNOWLEDGEMENTS

This work was funded by the High Energy Laser - Joint Technology Office (HEL-JTO) and administered through the Air Force Office for Scientific Research (AFOSR) under grant number FA9550-07-1-0574. The US government is authorized to reproduce and distribute reprints for government purposes notwithstanding any copyright notation thereon.

REFERENCES

- [1] M. Weng, A. Mani and S. Gordeyev, "Physics and Computation of Aero-Optics", *Annual Review of Fluid Mechanics*, Vol. **44**, pp. 299-321, 2012.
- [2] S. Gordeyev and E. Jumper, "Fluid Dynamics and Aero-Optics of Turrets", *Progress in Aerospace Sciences*, **46**, (2010), pp. 388-400.
- [3] R. M. Rennie, G. Crahan, E. Jumper, "Aerodynamic Design of an Aircraft-Mounted Pod for Improved Aero-Optic Performance", 48th AIAA Aerospace Sciences Meeting, 4-7 January 2010, Orlando, FL, AIAA Paper 2010-437.
- [4] E. Jumper, M. Zenk, S. Gordeyev, D. Cavalieri and M. Whiteley, "The Airborne Aero-Optics Laboratory, AAOL", Acquisition, Tracking, Pointing, and Laser Systems Technologies XXVI, Proceedings of SPIE, Volume **8395**, Paper 8395-6, June, 2012.
- [5] Whiteley, MR, Goorskey DJ, and Drye, R, "Aero-Optical Jitter Estimation Using Higher-Order Wavefronts", Acquisition, Tracking, Pointing, and Laser Systems Technologies XXVI, Proceedings of SPIE, Volume **8395**, Paper 8395-13, June, 2012.

- [6] C. Porter, S.Gordeyev, M. Zenk and E. Jumper,"Flight Measurements of Aero-Optical Distortions from a Flat-Windowed Turret on the Airborne Aero-Optics Laboratory (AAOL)", AIAA Paper 2011-3280.
- [7] Smith, AE, Gordeyev, S and Jumper, E, "Recent Measurements of Aero-Optical Effects Caused by Subsonic Boundary Layers", Acquisition, Tracking, Pointing, and Laser Systems Technologies XXVI, Proceedings of SPIE, Volume **8395**, Paper 8395-11, June, 2012.
- [8] S. Gordeyev, J.A. Cress, E. Jumper and A.B. Cain, "Aero-Optical Environment Around a Cylindrical Turret with a Flat Window", *AIAA Journal*, Vol. **49**, No. 2, pp. 308-315, 2011.
- [9] Ross, T. S. (2009). Limitations and applicability of the Maréchal approximation, *Applied Optics*, 48(10), 1812-1818.
- [10] S.Gordeyev, J. Cress and E. Jumper, "Far-Field Intensity Drop-Outs Caused by Turbulent Boundary Layers", DEPS, Beam Control Conference, 23-26 May, 2011, Orlando, FL. Paper 11-BC-050.
- [11] Goorskey, DJ, "Spatial And Temporal Characterization of AAOL Flight Test Data", Acquisition, Tracking, Pointing, and Laser Systems Technologies XXVI, Proceedings of SPIE, Volume **8395**, Paper 8395-8, June, 2012.